

# The Indian Ocean Geoid Low at a plume-slab overpass

Bernhard Steinberger<sup>a,b,\*</sup>, Samurdhika Rathnayake<sup>a,c</sup>, Elodie Kendall<sup>a</sup>

<sup>a</sup>GFZ German Research Centre for Geosciences, Telegrafenberg, 14473 Potsdam, Germany

<sup>b</sup>Centre for Earth Evolution and Dynamics, University of Oslo, PO Box 1028, 0315 Oslo, Norway

<sup>c</sup>Department of Land Surveying and Geo-Informatics, The Hong Kong Polytechnic University, 181 Chatham Road South, Kowloon, Hong Kong

---

## Abstract

The Indian Ocean Geoid Low (IOGL) appears as a prominent feature if the geoid is, as usual, shown with respect to the Earth's reference shape. However, if it is shown relative to hydrostatic equilibrium, i.e. including excess flattening, it appears as merely a regional low on a north-south trending belt of low geoid. For a mantle viscosity structure with an increase of 2-3 orders of magnitude from asthenosphere to lower mantle, which is suitable to explain the long-wavelength geoid, a geoid low can result from both positive density anomalies in the upper mantle and negative anomalies in the lower mantle. Here we propose that the IOGL can be explained due to a linear, approximately north-south-trending high-density anomaly in the lower mantle, which is crossed by a linear, approximately West-Southwest - East-Northeast trending anomaly low-density anomaly in the upper mantle. While the former can be explained due to its location in a region of former subduction and inbetween the two Large Low Shear Velocity Provinces (LLSVPs), we propose here that the latter is due to an eastward outflow from the Kenya plume rising above the eastern edge of the African LLSVP. We show that, with realistic assumptions we can approximately match the size, shape and magnitude of the geoid low.

**Keywords:** geoid, slab, plume, Africa, India

---

## 1. Introduction

Various sources which could give rise to the Indian Ocean Geoid Low (IOGL) have been proposed in the literature, including a low-density anomaly in the upper mantle (Reiss et al., 2017; Rao et al., 2020) and high-density anomaly in the lower mantle (Rao and Kumar, 2014), as both can cause a geoid low. Recently, Ghosh et al. (2017) have shown that the IOGL can be explained well by density anomalies inferred from seismic tomography, but the cause of these density anomalies was not thoroughly investigated. In this study, we pursue the idea stemming from Ghosh et al. (2017) that the IOGL occurs at the crossing point of a roughly north-south trending positive anomaly in the lower mantle (e.g. slabs from the “ring of fire”) and a roughly East-West to WSW-ENE trending negative anomaly in the upper mantle by developing a set of simple, synthetic geoid/density models.

The IOGL is only very prominent if you consider the geoid with respect to the reference shape (Figure 1, left). The geoid with respect to the hydrostatic equilibrium shape (second from left), which considers an excess flattening, features a much less prominent low which is just a local minimum along a belt stretching from the Antarctic to Arctic. After additionally correcting for the crust, which mostly has an effect around

---

\*Corresponding author; e-mail: bstein@gfz-potsdam.de, phone: +49-331-288-1881

36 Tibet, the IOGL appears even more connected to the geoid low under Asia (third from left). The right  
 37 panel also corrects for the isostatically compensated ridges. If one further corrects for the effects of upper  
 38 mantle slabs (Hager, 1984, not shown here), which, in this hemisphere, mainly “flattens” the geoid high  
 39 centered on New Guinea, the remaining “residual” geoid shows a very good correspondence with the Large  
 40 Low Shear Velocity Provinces (LLSVPs). Accordingly, the dominating large-scale structure of the residual  
 41 geoid, including the roughly NNW-SSE trending trough between the LLSVPs, can be well-explained from  
 42 lower-mantle density anomalies inferred from seismic tomography (Hager and Richards, 1989).

43 However, where could the proposed hot anomaly in the upper mantle, which would give rise to the IOGL  
 44 superposed on this large-scale trough originate from? To address this question, we consider that the IOGL  
 45 is slightly elongated towards East Africa, which could correlate with an outflow from the Kenya plume rising  
 46 from the margin of the African LLSVP, as imaged by current tomography models (Chang et al., 2020, 2015;  
 47 Durand et al., 2017; Boyce et al., 2021). As the LLSVP margin is overlain by many plumes and reconstructed  
 48 eruption locations of Large Igneous Provinces (LIPs) it has been proposed to be a “Plume Generation Zone”  
 49 (Burke et al., 2008). Evidence for a hot midmantle anomaly in the area of the IOGL has also been reported  
 50 by Reiss et al. (2017) who used the differential travel times of PP, SS waves and their precursors to find a  
 51 deepened 410 km discontinuity and elevated 660 km discontinuity. Rao et al. (2020) also reported a thin  
 52 mantle transition zone from 3-D time to depth migration of  $P$  receiver functions.

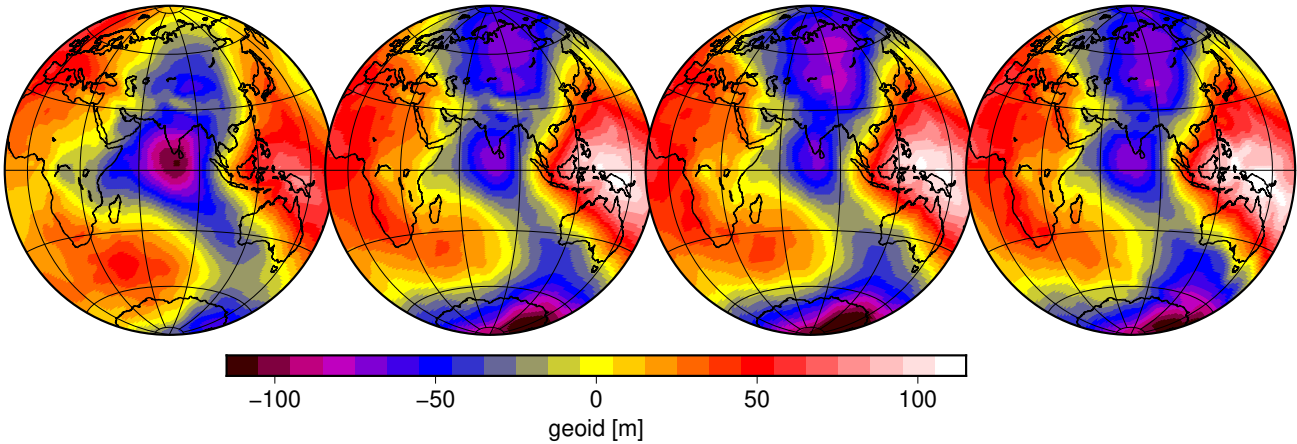


Figure 1: Observed geoid (Pavlis et al., 2012) from left to right (i) relative to reference shape, i.e. disregarding excess flattening (ii) relative to equilibrium spheroid (Nakiboglu, 1982) (iii) minus contribution down to the base of the crust derived from CRUST1.0 (Laske et al., 2013), and (iv) minus the effect of ocean floor age (Müller et al., 2008) following Steinberger (2016) and assuming isostatic compensation.

## 53 2. Methodology

54 Our geoid computations are based on mantle flow models expanded in spherical harmonics (Hager and  
 55 O’Connell, 1979, 1981) for radial viscosity variations only. In this case, the effect of density anomalies at a  
 56 given depth and spherical harmonic degree on the geoid can be expressed in terms of geoid kernels (Richards  
 57 and Hager, 1984; Ricard et al., 1984). Figure 2 shows that these kernels reverse sign in the lower mantle,

58 particularly for long wavelengths ( $\sim$ degree 2-5). In this way, a positive density anomaly in the lower part  
 59 of the mantle, and a negative density anomaly closer to the surface can give rise to a negative geoid. For  
 60 shorter wavelengths (degrees 6 and higher), the lower part of the mantle has a smaller contribution to the  
 61 observed geoid, and a negative geoid can result from both negative density anomalies at intermediate depths  
 62 (below  $\sim$ 200-300 km) and a positive anomaly at shallower depth. The combined effect of density anomalies  
 63 of different sizes and at various depth on the geoid is not straightforward and it is therefore important  
 64 to consider some simple synthetic density models to assess the dependence of the geoid on these various  
 65 parameters.

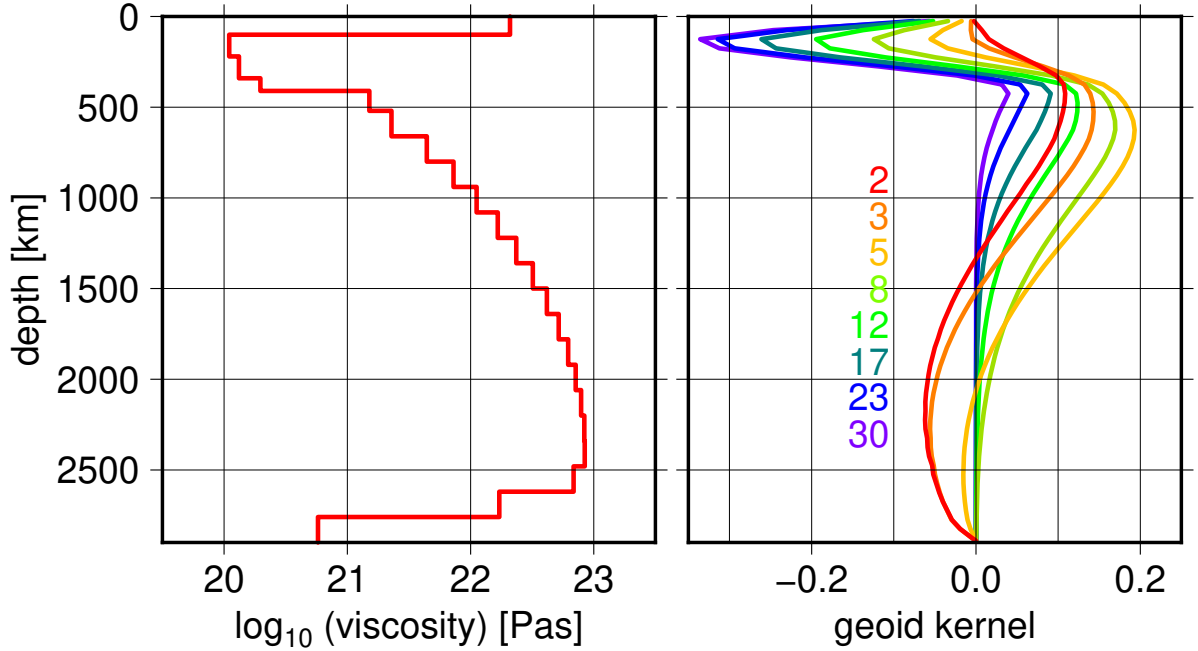


Figure 2: Left: reference viscosity structure from Steinberger (2016). Right: corresponding geoid kernels for spherical harmonic degrees 2, 3, 5, 8, 12, 17, 23, 30.

66 In particular we consider a high-density “ring” in the lower mantle and a low-density “streak” in the upper  
 67 mantle. In order to avoid sharp cutoffs which, after spherical harmonic expansion, can lead to “ringing”, i.e.  
 68 artificial small-scale fluctuations, we model these features with a cosine taper, i.e. for a half-width  $w/2$  the  
 69 density anomaly as a function of distance  $x$  from the center line is modelled as  $\rho(x) = \rho_0 \cdot (0.5 + 0.5 \cos(\pi x/w))$   
 70 for  $|x| < w$  and zero for  $|x| \geq w$ . For example, a half-width 7 degrees means the density anomaly has dropped  
 71 to half the centerline value at 7 degrees from the centerline, and to zero at 14 degrees from it. Additionally, we  
 72 apply a spectral cosine taper in the degree range 32-63 after expanding these features in spherical harmonics  
 73 until degree and order 63.

### 3. Results

Figure 3 shows one representative result. It has a high-density “ring” in the lower mantle (half-width 15 degrees, depth extent 1500-2600 km,  $\sim$  north - south, all around the Earth, along a great circle) and a low-density “streak” in the upper mantle (half-width 7 degrees, 100-400 km depth extent) from East Africa (30°E, where there is a large upwelling from the African LLSVP) towards East-Northeast until 120°E near the subduction zones.

The highest mantle viscosity likely lies in the depth range 1500–2600 km (Steinberger, 2016). At these depths, sinking rates reach a minimum and hence this region hosts most slabs. Slabs would also accumulate in the lowermost mantle, but there are indications that thermochemical piles also reside in the lowermost mantle with a positive density anomaly (Lau et al., 2017). Therefore we don’t consider density anomalies there, because it is not clear whether piles or slabs have a higher density.

A depth range of 100 to 400 km corresponds to the sublithospheric upper mantle, where the viscosity-depth profile is likely at a minimum (Steinberger, 2016). Optionally, the equilibrium effect of the olivine-spinel phase transition is also partially included. Effectively, with the phase boundary parameters chosen (Steinberger, 2007) the full effect of the phase transition corresponds to doubling the density anomaly for a 138 km thick layer. A thermal expansivity of  $2.8 \cdot 10^{-5}/\text{K}$ , which is approximately appropriate for that depth range (Steinberger and Calderwood, 2006; Schmeling et al., 2003) combined with a plume temperature anomaly of 250 K, corresponding to generic estimates (Schubert et al., 2001), yields a density anomaly of -0.7%.

The modelled geoid built with these parameters (Figure 3) reproduces the overall size and shape of the actual geoid low of  $\sim 30$  m (relative to the “saddle” to the north) or  $\sim 50$  m (relative to the “saddle” to the SE), on an extended roughly north-south trending geoid low well.

The dependence of the geoid on the size and depth range of the anomaly is illustrated in Figure 4. Here we consider high-density anomalies in the lower mantle and low-density anomalies in the upper mantle separately. To understand the resulting geoid, one has to consider that a low density anomaly by itself always causes a geoid low, but the resulting dynamic topography highs, both at the surface and core-mantle boundary (the latter playing a smaller role and being negligible for upper-mantle anomalies) cause a geoid high. The opposite is the case for high density anomalies. Because the respective low and high can have different width, with their relative width depending on viscosity structure, a rather complicated total anomaly, with a narrower high overlaying a wider low, can result.

The viscosity structure was chosen, such that a geoid prediction, based on seismic tomography, fits the observed geoid well (Steinberger, 2016). It has been shown that in this case, a negative geoid can result from both a low-density anomaly in the upper mantle, i.e. in this case the effect of the density itself is dominant and a high-density anomaly in the lower mantle, where hence the effect of the dynamic topography caused is dominant.

Yet for the upper mantle anomalies, a geoid high that is either narrower or wider, or even a combination of both, caused by the effect of dynamic topography is overlain. The narrower geoid high appears, relatively, most prominently for a comparatively thin streak and in cases where the anomaly is restricted to shallow



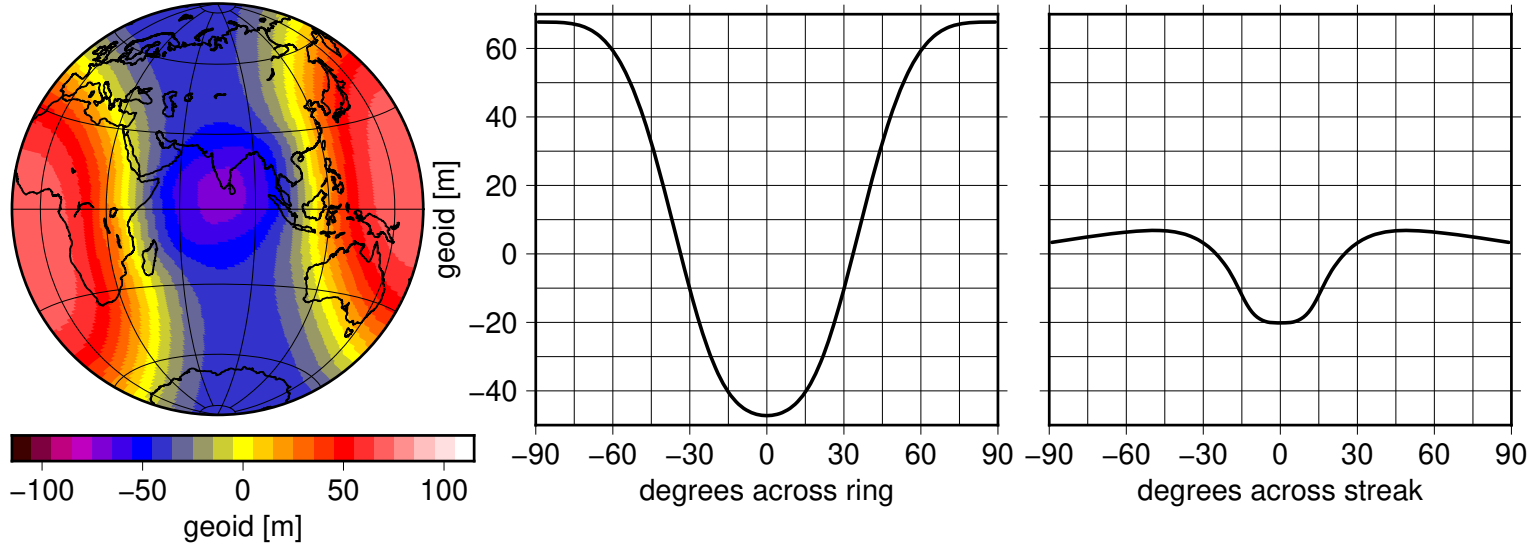


Figure 3: Modelled geoid map and profiles. 0.5 % density anomaly in a “ring” of half-width 15 degrees with cosine taper (i.e. reaching zero 30 degrees from the center line) in the depth range 1500 km to 2600 km, centered on a great circle with a pole at 10°S, 12°W, and -0.7 % anomaly in a “streak” of half-width 7 degrees with cosine taper in the depth range 100 km to 400 km and ranging from 30°E to 120°E, along a great circle with a pole at 70°N, 30°W. 50 % of the effect of the olivine-spinel phase transition is also considered, effectively assuming that the temperature anomaly at the phase transition has dropped to half. Effect of the phase transition is assigned to the 350-400 km depth layer, i.e. at 375 km depth. Map view for a combination of both, and profiles orthogonally across the center of each, separately.

depth. The fact that the actual geoid low does not feature a central high could indicate that the density anomaly is more prominent near the transition zone, as suggested in previous work (Reiss et al., 2017; Rao et al., 2020). The exothermic phase transition at around a depth of 410 km may further strengthen the effect of any temperature and density anomalies around that depth.

The width of the geoid low also depends on the width of the streak, albeit not proportionally: For example, for a narrow streak (e.g. 3 degrees half-width) the width of the geoid low can be much wider, with still about half the maximum value around 12 degrees from the center line. On the other hand, a wider streak gives rise to a geoid low of higher amplitude, but only slightly wider. We report that, for a realistic range of parameters, the modelled geoid amplitude ( $\sim 30$  m) matches the observed geoid well.

For the positive, lower mantle density anomaly, a narrower, central geoid high may occur due to the effect of the density anomaly itself. This high is more prominent for shallower anomalies, and for narrower rings. It does not occur if density anomalies are restricted to depths below 1800 km. The width of this geoid low is almost independent of the width of the high-density ring. Instead, the anomaly width almost only maps into the amplitude of the geoid low, with half the maximum value around 30 to 40 degrees from the center line. This can be explained because, for an anomaly in the mantle below 1000 km, the resulting topography low is dominated by the very longest wavelengths, regardless of the size of the anomaly itself.

## 4. Discussion

To assess whether this conceptual model could be realistic, we show in Figure 5 the present-day flow field at 262.5 km depth and average density in the upper mantle from a recent tomography-based model (Steinberger, 2016). Density is based on a combination of the SL2013SV model (Schaeffer and Lebedev, 2013) closer to the surface and a recent update of Grand (2002) deeper down, with a transition at 200 km depth, as the resolution of SL2013SV deteriorates at larger depth. It shows a series of low density material which, in combination with the arrows showing horizontal flow (10 degrees of arc arrow length = 5 cm/yr) could indicate an ENE outflow from the Kenya plume towards the southern tip of India. This is further visualized by a cross section through the same density and flow model (Figure 6).

This low density anomaly correlates well with a linear low S-velocity anomaly east of East Africa as seen in the votemap (Hosseini et al., 2018; Shephard et al., 2017) combining many tomographic models in Figure 7. The geometry of this low S-wave anomaly should be resolvable as most current global tomography models have a nominal lateral resolution of  $\sim 1000$  km. A flow field into the upper mantle beneath East Africa and in the upper mantle laterally away from the LLSVP is a persistent and robust feature of many models. Isosurfaces of low-velocity anomalies in current global tomography models such as SGLOBE-rani (Chang et al., 2015), SAVANI (Auer et al., 2014), SEISGLOB2 (Durand et al., 2017) and S362ANI (Kustowski et al., 2008) indicate that hot material may flow east to north-eastward from Kenya towards the mid-oceanic ridge and south of India (Figure 8). However, it is less clear for SEISGLOB2.

The pattern of density anomalies and flow field in Figure 5 indicates that the connection between the African superplume or Kenya plume and the Indian Ocean would be just north of Madagascar. Figures 5 and 7 suggest there is a region of thicker lithosphere beneath the Horn of Africa (Somalia), however, south of it and north of Madagascar there could be a “channel” for material to flow eastward towards the Indian Ocean. Maps of lithospheric thickness beneath Africa from elevation, geoid and thermal analysis (Figure 8, Globig et al., 2016) also show a region of thicker lithosphere North of Kenya, beneath the Horn of Africa and also west of Kenya, the Congo Craton. Flow may be diverted around regions of thick lithosphere and focussed in regions of thinner lithosphere, corresponding to the concept of upside down drainage (Sleep, 1997). The channeled flow eastward from the Kenya plume could be similar to the one proposed from the Afar plume towards the Gulf of Aden and a northward channel towards Arabia (e.g., Chang et al., 2020).

Mantle plumes can tilt due to plate motion and/or mantle wind (e.g., Skilbeck and Whitehead, 1978; Olson and Singer, 1985). Following the geodynamic modelling studies of plumes with and without the presence of mantle wind (Steinberger and Antretter, 2006; Richards and Griffiths, 1988) and with plate-like behaviour (e.g., Arnould et al., 2020), Davaille et al. (2005) and Chang et al. (2020) concluded it to be impossible to link the low velocity anomaly beneath South Africa to that beneath Afar (tilt  $\sim 45$  degrees). As the IOGL is further from South Africa than Afar, we find it more plausible that material is channeled in the upper mantle from the Kenya plume. However, in order to plausibly explain the size of the anomaly, it is necessary that, in the IOGL area the material not only occurs at the base of the lithosphere but reaches at least to 410 km depth. This could possibly be due to a downward pull induced by subducted slabs in the lower mantle.

166 This flow from the Kenya plume towards the IOGL would be part of a larger-scale “conveyor belt” (Becker  
167 and Faccenna, 2011) from an upwelling associated with the African LLSVP towards the Tethyan collisional  
168 belt with its subducted slabs. A transition from eastward towards more northeastward flow further east  
169 could be due to the strong northward component of the Indian plate motion dragging material along. This  
170 is in accord with observations of azimuthal anisotropy, which show a change in fast orientation from ENE  
171 to NNE at  $\sim 150$ -300 km depth (Yuan and Beghein, 2013).

172 The Kenya plume originates around 45 Ma as an upper bound (Ebinger et al., 1993; Nelson et al., 2012).  
173 With typical flow speeds of roughly about 5 cm/yr this would then correspond to 2250 km total flow, which  
174 is not quite enough to reach the IOGL. But of course, flow speeds are uncertain and might also be faster,  
175 in particular for hot and low-viscosity plume material - this computation doesn’t consider lateral viscosity  
176 variations.

177 Another possible source of hot material below the IOGL is from the Réunion plume (Ghosh et al., 2017).  
178 This plume is older (around 65 Ma) and closer to the IOGL, and it was initially located beneath the Indian  
179 plate, which could have aided in dragging hot material along. However, mantle flow streamlines from La  
180 Réunion (Figure 5) end up further south. In light of this and because the IOGL has an extension towards  
181 East Africa, we consider the Kenya plume a more likely source.

182 For the results shown in this paper, we only consider one specific viscosity model (Figure 2), but mantle  
183 viscosity structure is uncertain with a wide variety of models recently proposed. We consider it sufficient for  
184 our purpose, though, to use a viscosity model that is suitable to explain the global geoid (Steinberger, 2016).  
185 In this case, the geoid predicted based on the synthetic density models used here can also be considered  
186 realistic. Obviously, with an otherwise poorly constrained viscosity model we cannot tightly constrain the  
187 density models responsible for the geoid low. Our goal is merely to propose a model that is dynamically  
188 reasonable and not in obvious conflict with other evidence.

## 189 5. Conclusions

190 Recently, evidence from seismic tomography and observations of a thinned transition zone suggest that  
191 the IOGL is, at least partly, caused by the presence of hot low-density material in the upper mantle and  
192 transition zone. Yet previous suggestions that a low geoid in the region may be caused by the presence of cold  
193 high-density slabs in the lower mantle are still valid. Here we build upon these ideas and show that a nearly  
194 circular geoid low can be the result of the superposition of two nearly orthogonal geoid troughs, for example  
195 one due to slabs in the lower mantle and one due to hot material in the upper mantle. By constructing  
196 synthetic density models with realistic assumptions, we show that the size, shape and amplitude of the IOGL  
197 can all be matched well.

198 We propose an origin of the hot material from an upwelling plume from the eastern margin of the  
199 African LLSVP. Large-scale global flow models indicate that material flows from the LLSVP towards the  
200 upper mantle beneath East Africa and then is possibly channeled further in an east/north-easterly direction  
201 towards the South of India. Dynamical models also suggest that a strong tilt of the plume itself, towards  
202 the IOGL, is unlikely, and that flow rather follows the base of the lithosphere. We regard the Kenya plume

as the most likely candidate for the origin of the hot material. This plume has recently been imaged as a feature separate from the Afar plume, at least in the upper mantle, rising from the African LLSVP. Since the Afar plume likely feeds into the rifts of the Red Sea and Gulf of Aden, material from the Kenya plume would have to feed elsewhere. Flow from the Kenya plume is likely to be partially obstructed by blocks of thick lithosphere, especially around the Horn of Africa. Yet there appears to be comparatively thin lithosphere south of it, and north of Madagascar, where outflow towards the East could occur. Such an outflow, and continuously hot material towards the IOGL is also evidenced by seismic tomography.

## Acknowledgements

This work was partially funded by the Research Council of Norway Centre of Excellence Project 223272. Additional funding was provided from the innovation pool of the Helmholtz Association through the Advanced Earth System Modelling Capacity (ESM) activity.

## References

- Arnould, M., Coltice, N., Flament, N., Mallard, C., 2020. Plate tectonics and mantle control on plume dynamics. *Earth Planet. Sci. Lett.* 547, 116439. doi:10.1016/j.epsl.2020.116439.
- Auer, L., Boschi, L., Becker, T.W., Nissen-Meyer, T., Giardini, D., 2014. Savani: A variable resolution whole-mantle model of anisotropic shear velocity variations based on multiple data sets. *J. Geophys. Res. - Sol. Ea.* 119, 3006–3034. doi:10.1002/2013JB010773.
- Becker, T.W., Faccenna, C., 2011. Mantle conveyor beneath the tethyan collisional belt. *Earth Planet. Sci. Lett.* 310, 453–461. doi:10.1016/j.epsl.2011.08.021.
- Boyce, A., Bastow, I.D., Cottaar, S., Kounoudis, R., De Courbeville, J.G., Caunt, E., Desai, S., 2021. Afrp20: New p-wavespeed model for the african mantle reveals two whole-mantle plumes below east africa and neoproterozoic modification of the tanzania craton. *Geochemistry, Geophysics, Geosystems* n/a, e2020GC009302. doi:10.1029/2020GC009302.
- Burke, K., Steinberger, B., Torsvik, T.H., Smethurst, M.A., 2008. Plume Generation Zones at the margins of Large Low Shear Velocity Provinces on the the Core-Mantle Boundary. *Earth Planet. Sci. Lett.* 265, 49–60. doi:10.1016/j.epsl.2007.09.042.
- Chang, S.J., Ferreira, A.M.G., Ritsema, J., van Heijst, H.J., Woodhouse, J.H., 2015. Joint inversion for global isotropic and radially anisotropic mantle structure including crustal thickness perturbations. *J. Geophys. Res. - Sol. Ea.* 120, 4278–4300. doi:10.1002/2014JB011824.
- Chang, S.J., Kendall, E., Davaille, A., Ferreira, A.M.G., 2020. The evolution of mantle plumes in East Africa. *J. Geophys. Res. - Sol. Ea.* 125, e2020JB019929. doi:10.1029/2020JB019929.
- Davaille, A., Stutzmann, E., Silveira, G., Besse, J., Courtillot, V., 2005. Convective patterns under the Indo-Atlantic box. *Earth Planet. Sci. Lett.* 239, 233–252. doi:10.1016/j.epsl.2005.07.024.

236 Durand, S., Debayle, E., Ricard, Y., Zaro, C., Lambotte, S., 2017. Confirmation of a change in the global  
 237 shear velocity pattern at around 1000 km depth. *Geophys. J. Int.* 211, 1628–1639. doi:10.1093/gji/ggx405.

238 Ebinger, C.J., Yemane, T., Woldegabriel, G., Aronson, J.L., Walter, R.C., 1993. Late Eocene-recent  
 239 volcanism and faulting in the southern main Ethiopian rift. *J. Geol. Soc. London* 150, 99–108.  
 240 doi:10.1144/gsjgs.150.1.0099.

241 Ghosh, A., Thyagarajulu, G., Steinberger, B., 2017. The importance of upper mantle heterogeneity in  
 242 generating the Indian Ocean geoid low. *Geophys. Res. Lett.* 44, 9707–9715. doi:10.1002/2017GL075392.

243 Globig, J., Fernndez, M., Torne, M., Vergs, J., Robert, A., Faccenna, C., 2016. New insights into the crust  
 244 and lithospheric mantle structure of Africa from elevation, geoid, and thermal analysis. *J. Geophys. Res.*  
 245 - *Sol. Ea.* 121, 5389–5424. doi:10.1002/2016JB012972.

246 Grand, S.P., 2002. Mantle shear-wave tomography and the fate of subducted slabs. *Phil. Trans. R. Soc.*  
 247 *Lond. A* 360, 2475–2491. doi:10.1098/rsta.2002.1077.

248 Hager, B.H., 1984. Subducted slabs and the geoid: constraints on mantle rheology and flow. *J. Geophys.*  
 249 *Res.* 89, 6003–6015.

250 Hager, B.H., O’Connell, R.J., 1979. Kinematic models of large-scale flow in the Earth’s mantle. *J. Geophys.*  
 251 *Res.* 84, 1031–1048. doi:10.1029/JB084iB03p01031.

252 Hager, B.H., O’Connell, R.J., 1981. A simple global model of plate dynamics and mantle convection. *J.*  
 253 *Geophys. Res.* 86, 4843–4867. doi:10.1029/JB086iB06p04843.

254 Hager, B.H., Richards, M.A., 1989. Long-wavelength variations in earth’s geoid: physical models and  
 255 dynamical implications. *Philosophical Transactions of the Royal Society of London. Series A, Mathematical*  
 256 *and Physical Sciences* 328, 309–327. doi:10.1098/rsta.1989.0038.

257 Hosseini, K., Matthews, K.J., Sigloch, K., Shephard, G.E., Domeier, M., Tsekhmistrenko, M., 2018. Sub-  
 258 Machine: Web-Based tools for exploring seismic tomography and other models of Earth’s deep interior.  
 259 *Geochem., Geophys., Geosys.* 19, 1464–1483. doi:10.1029/2018GC007431.

260 Kustowski, B., Ekström, G., Dziewoński, A.M., 2008. Anisotropic shear-wave velocity structure of the  
 261 Earth’s mantle: A global model. *J. Geophys. Res.* 113, B06306. doi:10.1029/2007JB005169.

262 Laske, G., Masters, G., Ma, Z., Pasyanos, M., 2013. Update on CRUST1.0 - a 1-degree global model of  
 263 Earth’s crust. *Geophys. Res. Abstr.* 15. Abstract EGU2013-2658.

264 Lau, H., Mitrovica, J.X., Davis, J.L., Tromp, J., Yang, H.Y., Al-Attar, D., 2017. Tidal tomography constrains  
 265 Earths deep-mantle buoyancy. *Nature* 551, 321–326. doi:10.1038/nature24452.

266 Müller, R.D., Sdrolias, M., Gaina, C., Roest, W.R., 2008. Age, spreading rates, and spreading asymmetry  
 267 of the world’s ocean crust. *Geochem., Geophys., Geosys.* 9, Q04006. doi:10.1029/2007GC001743.

268 Nakiboglu, S.M., 1982. Hydrostatic theory of the Earth and its mechanical implications. *Phys. Earth Planet.*  
269 *Inter.* 28, 302–311. doi:10.1016/0031-9201(82)90087-5.

270 Nelson, W.R., Furman, T., van Keken, P.E., Shirey, S.B., Hanan, B.B., 2012. Os-Hf isotopic insight  
271 into mantle plume dynamics beneath the East African Rift system. *Chem. Geol.* 320–321, 66–79.  
272 doi:10.1016/j.chemgeo.2012.05.020.

273 Olson, P., Singer, H., 1985. Creeping plumes. *J. Fluid Mech.* 158, 511–531. doi:10.1017/s0022112085002749.

274 Pavlis, N.K., Holmes, S.A., Kenyon, S.C., Factor, J.K., 2012. The development and evaluation of the Earth  
275 Gravitational Model 2008 (EGM2008). *J. Geophys. Res.* 117, B04406. doi:10.1029/2011JB008916.

276 Rao, B.P., Kumar, M.R., 2014. Seismic evidence for slab graveyards atop the Core Mantle Boundary beneath  
277 the Indian Ocean Geoid Low. *Phys. Earth Planet. Inter.* 236, 52–59. doi:10.1016/j.pepi.2014.08.005.

278 Rao, B.P., Kumar, M.R., Saikia, D., 2020. Seismic evidence for a hot mantle transition zone beneath the  
279 Indian Ocean Geoid Low. *Geochem., Geophys., Geosys.* 21, e2020GC009079. doi:10.1029/2020GC009079.

280 Reiss, A.S., Thomas, C., van Driel, J., Heyn, B., 2017. A hot midmantle anomaly in the area of the Indian  
281 Ocean Geoid Low. *Geophys. Res. Lett.* 44, 6702–6711. doi:10.1002/2017GL073440.

282 Ricard, Y., Fleitout, L., Froidevaux, C., 1984. Geoid heights and lithospheric stresses for a dynamic Earth.  
283 *Ann. Geophys.* 2, 267–286.

284 Richards, M.A., Griffiths, R.W., 1988. Deflection of plumes by mantle shear flow: Experimental results and  
285 a simple theory. *Geophys. J.* 94, 367–376. doi:10.1111/j.1365-246x.1988.tb02260.x.

286 Richards, M.A., Hager, B.H., 1984. Geoid anomalies in a dynamic Earth. *J. Geophys. Res.* 89, 5987–6002.  
287 doi:10.1029/JB089iB07p05987.

288 Schaeffer, A., Lebedev, S., 2013. Global shear speed structure of the upper mantle and transition zone.  
289 *Geophys. J. Int.* 194, 417–449. doi:10.1093/gji/ggt095.

290 Schmeling, H., Marquart, G., Ruedas, T., 2003. Pressure- and temperature-dependent thermal expan-  
291 sivity and the effect on mantle convection and surface observables. *Geophys. J. Int.* 154, 224–229.  
292 doi:10.1046/j.1365-246X.2003.01949.x.

293 Schubert, G., Turcotte, D.L., Olson, P., 2001. *Mantle Convection in the Earth and Planets.* Cambridge  
294 University Press.

295 Shephard, G.E., Matthews, K.J., Hosseini, K., Domeier, M., 2017. On the consistency of seismically imaged  
296 lower mantle slabs. *Scientific Reports* 7, 10976. doi:10.1038/s41598-017-11039-w.

297 Skilbeck, J.N., Whitehead, J.A.J., 1978. Formation of discrete islands in linear island chains. *Nature* 272,  
298 499–501. doi:10.1038/272499a0.

299 Sleep, N.H., 1997. Lateral flow and ponding of starting plume material. *J. Geophys. Res. - Sol. Ea.* 102,  
300 10001–10012. doi:10.1029/97JB00551.

301 Steinberger, B., 2007. Effect of latent heat release at phase boundaries on flow in the Earth's mantle, phase  
302 boundary topography and dynamic topography at the Earth's surface. *Phys. Earth Planet. Inter.* 164,  
303 2–20. doi:10.1016/j.pepi.2007.04.021.

304 Steinberger, B., 2016. Topography caused by mantle density variations: observation-based estimates  
305 and models derived from tomography and lithosphere thickness. *Geophys. J. Int.* 205, 604–621.  
306 doi:10.1093/gji/ggw040.

307 Steinberger, B., Antretter, M., 2006. Conduit diameter and buoyant rising speed of mantle plumes: Implica-  
308 tions for the motion of hot spots and shape of plume conduits. *Geochem., Geophys., Geosys.* 7, Q11018.  
309 doi:10.1029/2006GC001409.

310 Steinberger, B., Calderwood, A.R., 2006. Models of large-scale viscous flow in the Earth's mantle  
311 with constraints from mineral physics and surface observations. *Geophys. J. Int.* 167, 1461–1481.  
312 doi:10.1111/j.1365-246X.2006.03131.x.

313 Yuan, K., Beghein, C., 2013. Seismic anisotropy changes across upper mantle phase transitions. *Earth*  
314 *Planet. Sci. Lett.* 374, 132–144. doi:10.1016/j.epsl.2013.05.031.





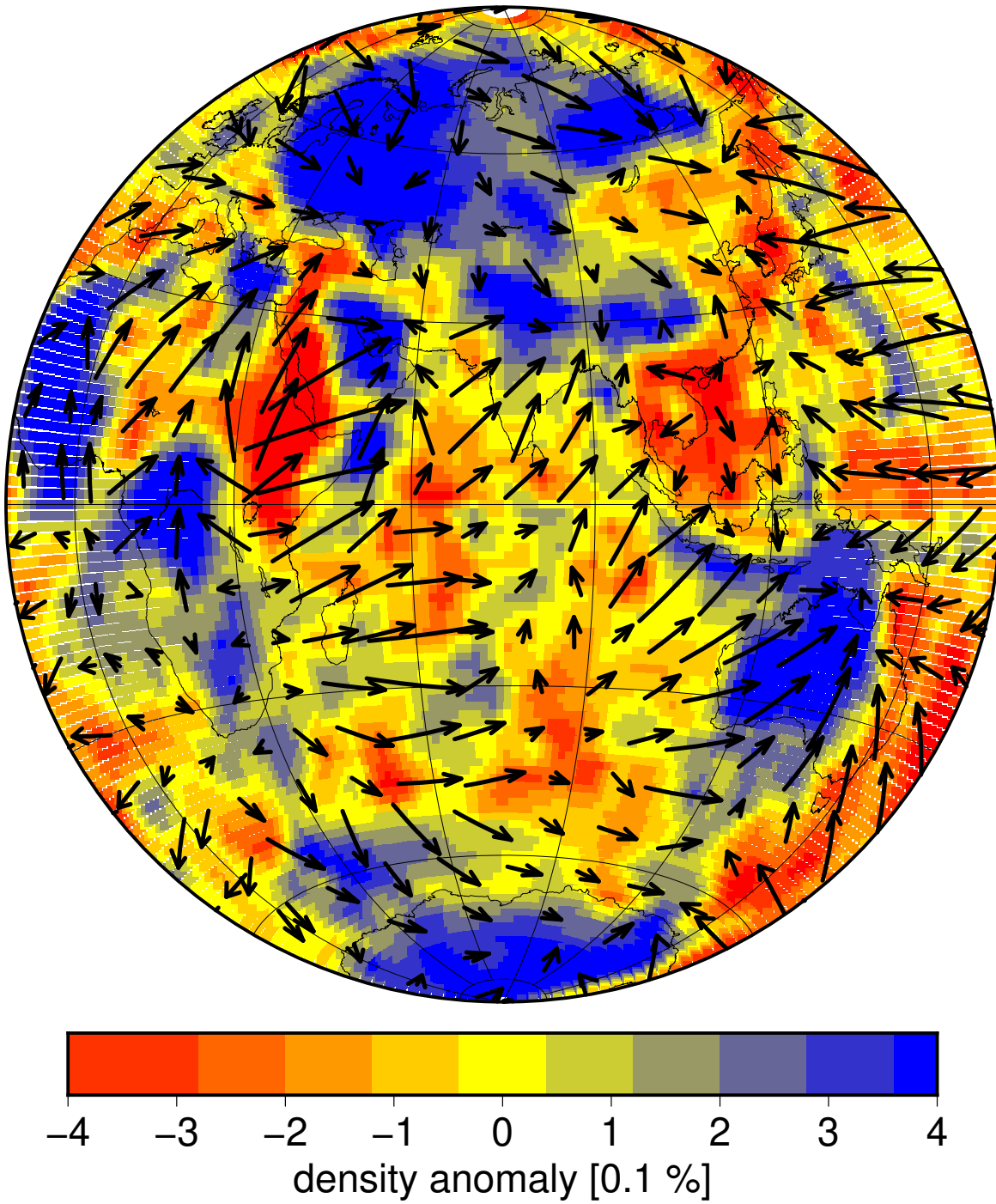


Figure 5: Average density in the depth range 100-400 km and flow field at depth 262.5 km for the reference model of Steinberger (2016).

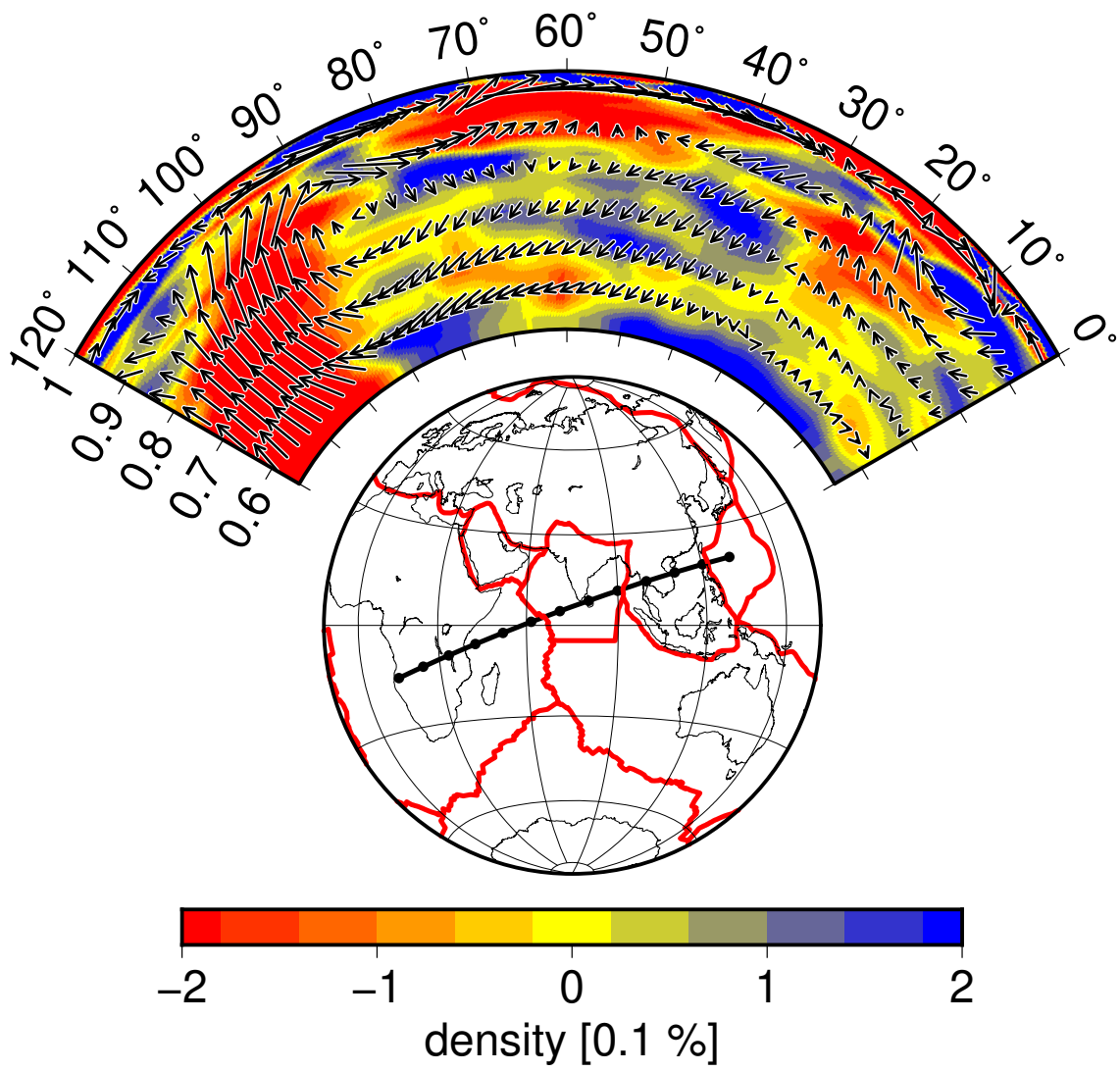


Figure 6: Vertical cross section through flow and density field for the reference model of Steinberger (2016).

300 km

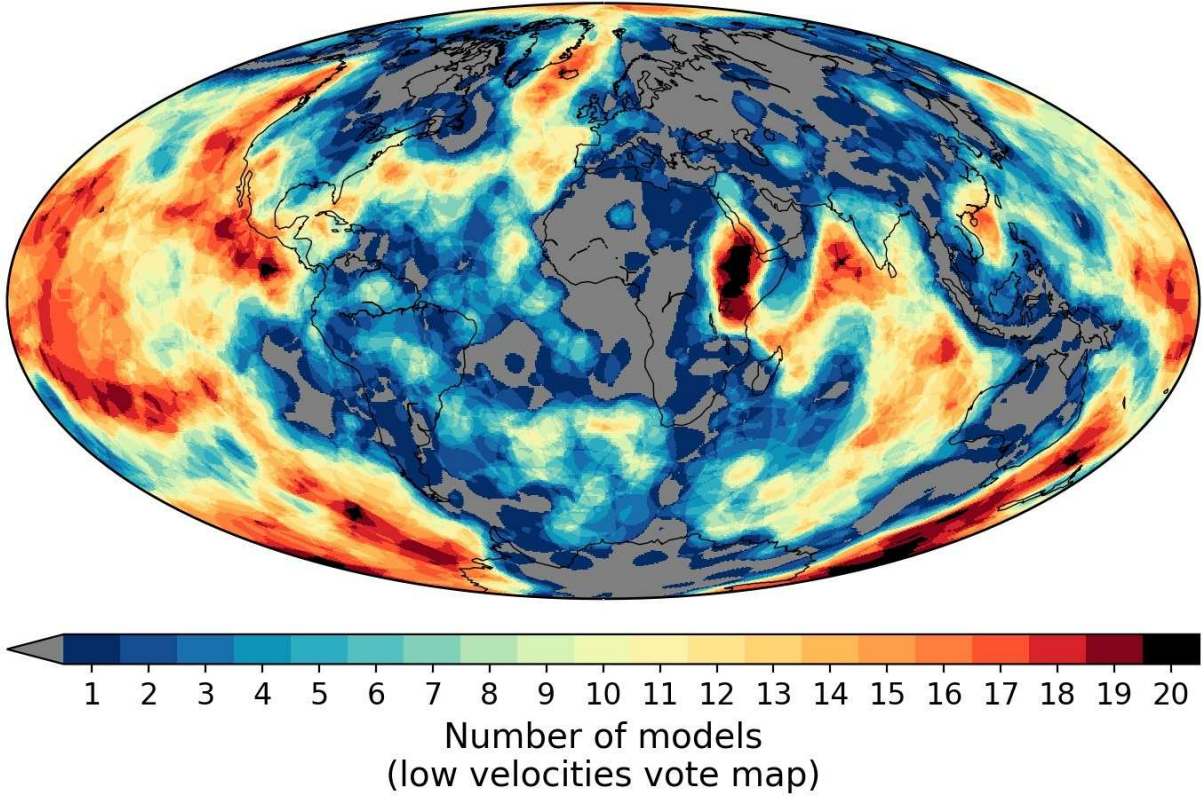


Figure 7: Votemap of all s-velocity models included by Hosseini et al. (2018) and  $|\text{velocities}| \geq \text{std.}$

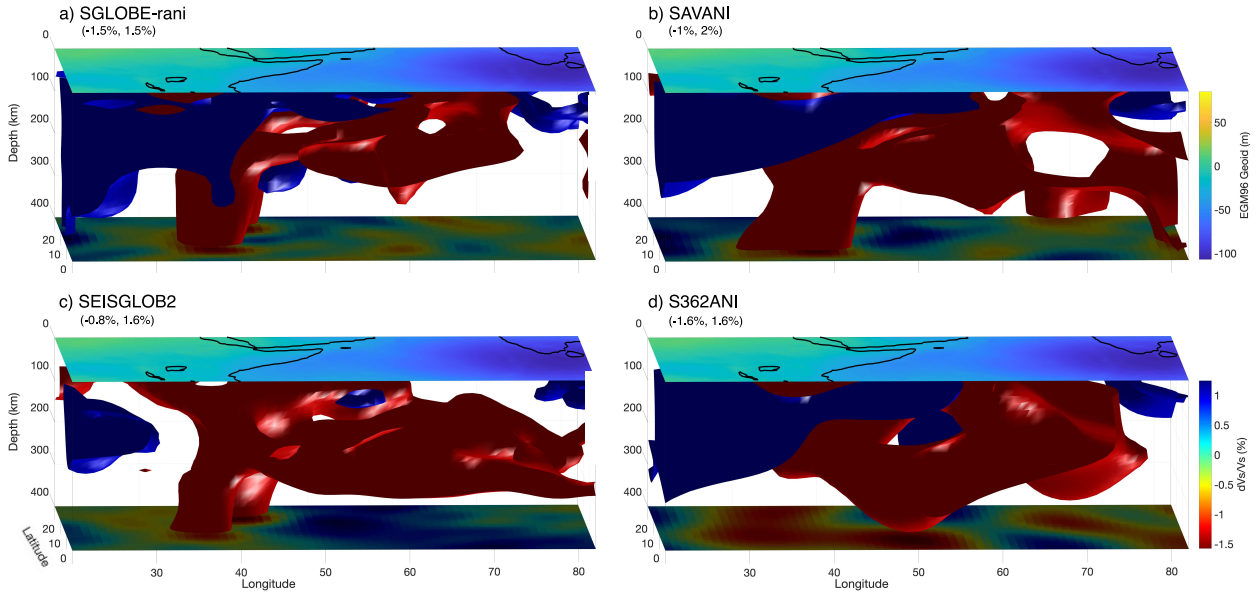


Figure 8: Isosurfaces of low- and high-velocity anomalies in the upper mantle beneath East Africa and the Indian Ocean from four global tomography models; SGLobe-rani (Chang et al., 2015), SAVANI (Auer et al., 2014), SEISGLOB2 (Durand et al., 2017) and S362ANI (Kustowski et al., 2008). We used different values for isosurfaces in each model to clearly show the lowest-velocity anomalies, which are noted on the top left of each subplot.